

Exploring transport mechanisms in an atomic precision advanced manufacturing (APAM) enabled pn junctions

J.P. Mendez,^{1, a)} X. Gao,^{1, b)} J. Ivie,¹ J.H.G Owen,² W.P. Kirk,³ J.N. Randall,² and S. Misra^{1, c)}

¹⁾*Sandia National Laboratories, 1515 Eubank SE, Albuquerque, NM 87123, USA*

²⁾*Zyvox Labs LLC, 1301 N. Plano RD, Richardson, TX 7508, USA*

³⁾*3D Epitaxial Technologies, LLC, 999 E. Arapaho Rd, Richardson, TX 75081, USA*

(Dated: October 24, 2024)

We investigate the different transport mechanisms that can occur in atomically precise advanced-manufacturing (APAM) pn junction devices at cryogenic and room temperatures. We first elucidate the potential cause of the anomalous behaviors observed in the forward-bias response of these devices in recent cryogenic temperature measurements, which deviates from the theoretical response of a silicon Esaki diode. Specifically, the suppression of the tunneling current at low bias and the appearance of regular diode current at lower biases than theoretically expected for silicon. We find that the latter can be attributed to modifications in the electronic band structure within the δ -layer regions, leading to band-gap narrowing induced by the high density of dopants. We also find that a combination of two sets of band-to-band tunneling (BTBT) parameters can qualitatively approximate the shape of the tunneling current at low bias. This can arise from band quantization and realignment due to the strong potential confinement in APAM-doped layers. Finally, we extend our analyses to room temperature operation, and we predict that trap-assisted tunneling (TAT) may become significant, leading to a complex superposition of BTBT and TAT transport mechanisms in the electrical measurements.

I. INTRODUCTION

Atomic precision advanced manufacturing (APAM) technology enables the creation of 2D doped regions, also known as δ -layers, in semiconductors with single-atom precision¹⁻⁵ and high conductivity⁶⁻¹¹. APAM has various applications, including the exploration of novel electronic devices for classical computing and sensing systems^{10,12-15}, or the exploration of dopant-based qubits in silicon, with recent advancements in understanding the advantages of leveraging the number of dopants as a degree of freedom^{16,17}, or the exploration of many body¹⁸ and topological¹⁹ effects in dopant chains. To date, nearly all of these devices have been made with donors^{12,13,15,17-19}. Recently, Ref. 10 reported the fabrication of the first APAM bipolar device, composed of a boron δ -layer and a phosphorus δ -layer embedded in silicon. Interestingly, the characteristic response of the device deviates from the theoretically expected behavior of a Si Esaki diode.

Fig. 1 shows the measured current-voltage (I-V) curves in the forward and reverse operation regimes at different temperatures. The authors of the paper speculated on the main transport mechanisms for these regions: (i) region 1 is due to increased band-to-band tunneling (BTBT) (a.k.a, Zener tunneling) under a reverse voltage bias; (ii) region 2 may be due to band misalignment between the two δ layers or non-ideal contact effect or localization effect in the boron δ -layer; (iii) region 3 is due

to increased BTBT under a forward voltage bias; (iv) region 4 is due to decreased BTBT under forward bias; (v) region 5 is dominated by the above-threshold current conduction as in a normal pn diode. We also note that, in region 5, the diode operates as a resistor, resulting in a linear current-voltage response, which appears as a linear curve in (a) and as a flatter curve on the logarithmic current scale in (b). Additionally, as the temperature is increased, the conductivity through the enclosing substrate start to conduct, increasing overall the current, as shown in the figure. From these results, we distinguish two qualitative differences between the measured data and that expected theoretical behavior from a Si Esaki diode - the suppression of BTBT in region 2²⁰⁻²² and the relatively low voltage for the onset of region 5 (at below 0.6 V) compared to the theoretical value in silicon diodes (approximately at 1.0 V) at cryogenic temperature.

In this work, we use semi-classical Technology Computer Aided Design (TCAD) to model different transport mechanisms expected for this structure, specifically to identify whether the unusual features in the I-V curves can be traced to the novel electronic properties of the δ layers. We have found that the measured low voltage onset in region 5 can be produced by the narrower band gap expected for APAM-doped silicon. We have also found that a combination of two sets of BTBT parameters can qualitatively approximate the shape of the tunneling current at low bias. This sheds light on a plausible cause of the atypical behavior, which is attributed to the quantization of the valence and conduction band structures in the p-type and n-type δ -layers, respectively, due to the confinement of the dopants in one direction. This intriguing result may also be relevant for other tunnel diode systems, such as those involving 2D material or

^{a)}jpmende@sandia.gov

^{b)}xngao@sandia.gov

^{c)}smisra@sandia.gov

van der Waals material, where a high density of electrons and holes are strongly confined in 2D planes. We further extend the models to include transport mechanisms that will appear at elevated temperatures, and provide predictions of the behavior expected by APAM pn devices at room temperature. We have found that trap-assisted tunneling (TAT) may become significant at room temperature, leading to a complex superposition of BTBT and TAT transport mechanisms in electrical measurements.

In the following, we describe our simulation approach in Sec. II, explore major transport mechanisms at low temperatures and compare our results with available experimental data in Sec. III, investigate additional mechanisms that may occur at room temperature in Sec. IV, and summarize our final findings in Sec. V.

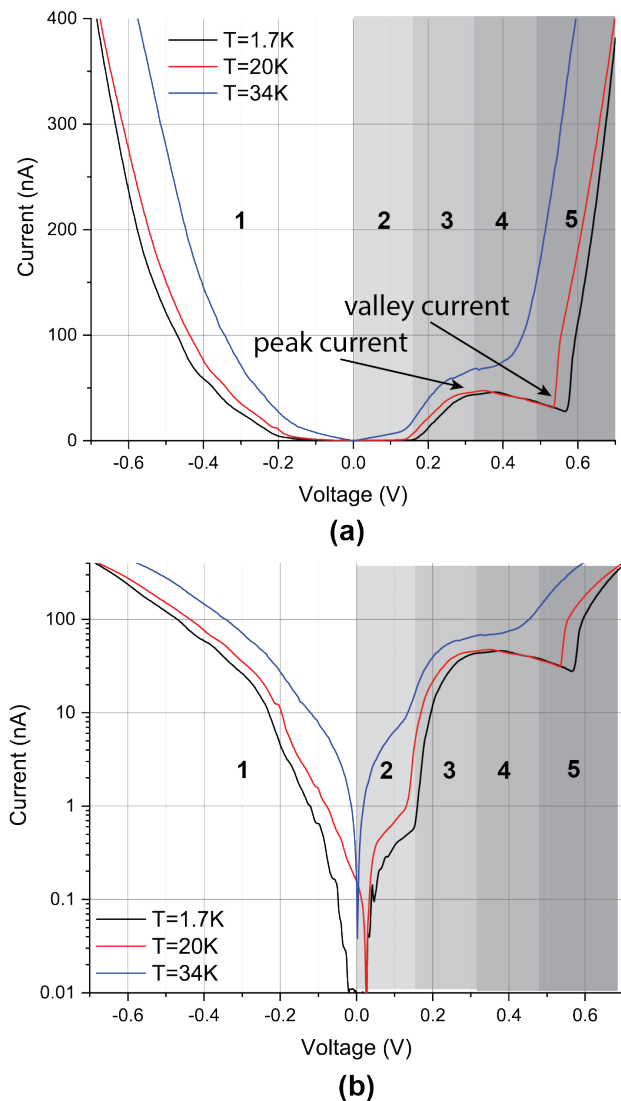


Figure 1. Measured current-voltage curves from Ref. 10: (a) linear plot and (b) semilogarithmic plot. The δ -layer width is 100 nm. Note that the measured current, as shown in (a) and (b), represents the absolute current.

II. SIMULATION APPROACH

In this work, we used the open-source TCAD code, Charon²³, which is a multi-dimensional, MPI-parallel, semi-classical device simulation code developed at Sandia National Laboratories. It is commonly argued that quantum mechanical modeling²⁴ is needed to model APAM devices due to sharp potential confinement in an APAM δ layer. However, recent work^{14,25} shows that semi-classical Charon simulations can capture the key current-voltage characteristics in APAM devices. For example, Ref. 25 shows that Charon simulations reproduce measured sheet resistances very well when proper mobility values are used in APAM phosphorous δ layers, and Ref. 14 shows that Charon simulations can predict the expected transistor-like current-voltage response in a proposed APAM vertical tunneling field effect transistor (v-TFET). In addition, it is well-known that a semi-classical TCAD simulation runs much quicker than a full quantum simulation and can be used to simulate complex device geometries.

Sandia's TCAD Charon code solves the Poisson equation, the continuity equations for electrons/holes/ions, and the lattice temperature equation. These partial differential equations can be solved individually or coupled together, using either finite element^{26,27} or finite volume discretization schemes²⁸. Device geometries and meshes are generated using the geometry and meshing tool called Cubit²⁹. Device simulation results are visualized using the open-source data analysis and visualization tool called Paraview³⁰.

Charon contains many advanced material models such as the BTBT model and trap-assisted tunneling (TAT) model (refer to Appendix A for the TAT model). In Charon, BTBT is modeled as a field-dependent generation rate which is given by^{31,32}

$$G_{bttt} = \alpha A \left(\frac{|F - F_{eq}|}{F_{eq}} \right)^\beta \left(\frac{F}{F_0} \right)^\gamma \exp\left(-\frac{B}{F}\right). \quad (1)$$

where G_{bttt} is in unit of $\text{cm}^{-3}\text{s}^{-1}$, F is the electric field magnitude in V/cm , and γ and β are fitting parameters. A and B are related to material properties such as effective masses and band-gap energy³³⁻³⁵, but they are often used as fitting parameters. These parameters were expressed for direct tunneling in Refs 33-35 as

$$A = \left(\frac{gm_r^{1/2}(qF_0)^2}{\pi h^2 E_g^{1/2}} \right) \quad (2)$$

and

$$B = \left(\frac{\pi^2 m_r^{1/2} E_g^{3/2}}{qh} \right), \quad (3)$$

where g is a degenerate factor, m_r is the reduced tunneling mass, q is the elementary charge, h is the Planck's constant and E_g is the bandgap. It was found in Ref. 31 that $\gamma = 2$ for direct transitions and $\gamma = 2.5$ for indirect

transitions, namely, phonon-assisted band-to-band tunneling. F_0 is equal to 1 V/cm. The value of α can be -1, or 1. When $\alpha = -1$, we have $G_{btt} < 0$, which indicates the BTBT is a recombination process. When $\alpha = 1$, we have $G_{btt} > 0$, which indicates the BTBT is a generation process. F_{eq} is the simulated, position-dependent electric field magnitude in a device at a zero-current equilibrium condition. The field factor, $(|F - F_{eq}|/F_{eq})^\beta$, theoretically guarantees zero current in equilibrium condition.

Silicon is known to be an indirect bandgap semiconductor material, however, it has been shown experimentally^{10,36-40} and theoretically⁴¹⁻⁴⁵ that silicon doped with extreme doses of P, beyond the solubility limit, becomes a direct bandgap material. Thus, for our calculations, we opted for a γ value of 2.0, substantiated by the existence of direct band-to-band tunneling in the measured IV in Ref. 10 at cryogenic temperature; indirect band-to-band tunneling would be impractical at low temperatures due to the absence of phonon-assisted tunneling process.

For the simulations, we also utilize the standard Arora mobility model for electrons and holes⁴⁶, the Slotboom model for intrinsic concentration⁴⁷, mid-gap Shockley-Read-Hall (SRH) and Auger recombination models. Table I includes the electron and holes mobilities predicted by the Arora model as function of the temperature for a doping density of $3 \times 10^{20} \text{ cm}^{-3}$. We note that Arora model overestimates the mobilities for very low temperatures. Therefore, in this work, we used Arora mobility model for room-temperature studies and the measured mobility in Refs. 6 and 10 for low-temperature studies. The table also includes the band gap and the electron affinity at different temperatures. We note that the computed band gap is lower than that of intrinsic silicon due to the effects of the dopants, as described by the Slotboom model. For more details of these models, we refer to the Charon's manual⁴⁸.

III. LOW-TEMPERATURE TRANSPORT MECHANISM

For our low-temperature simulations, we employ the 2D structure shown in Fig. 2, which consists of a p-type δ -layer with boron (B) dopants and a n-type δ -layer with phosphorous (P) dopants embedded in silicon, known as APAM pn junction. The δ layers are approximated by highly-doped layers with thicknesses of 4 nm. The p-type and n-type δ -layers make direct Ohmic contact with the anode and cathode contacts, respectively. From our experimental observations⁴⁹, electrons and holes freeze out in the Si cap and Si substrate layers at low temperatures (below 50 Kelvin), and thus, the carrier transport mainly occurs across the δ -layers. Therefore, to avoid unintended leakage paths in our simulations, we chose to place Ohmic contacts directly at the end of the δ -layers for low-temperature simulations, as shown in Fig. 2. An analysis of contact configuration with the δ -layers are included in Sec. IV B at room temperature. The voltage is applied to

the anode contact, while the cathode contact is grounded. We chose doping densities of $3 \times 10^{20} \text{ cm}^{-3}$ in the δ -layers, and an acceptor density of $N_A = 1 \times 10^{17} \text{ cm}^{-3}$ in the Si substrate and Si cap. These doping densities and thicknesses are chosen to reproduce the main characteristics of the fabricated device in Ref.10; with the δ -layer thicknesses being defined as 4 nm and the doping densities in the δ layers as $3 \times 10^{20} \text{ cm}^{-3}$, this approximately results in the measured sheet doping density in the δ -layers of $1.2 \times 10^{14} \text{ cm}^{-2}$. Additionally, the bipolar device is enclosed in intrinsic silicon, thus, in our simulations, we chose doping densities for the substrate and the cap that are several orders of magnitude lower than those in the δ -layers as not to alter the electrostatic potential.

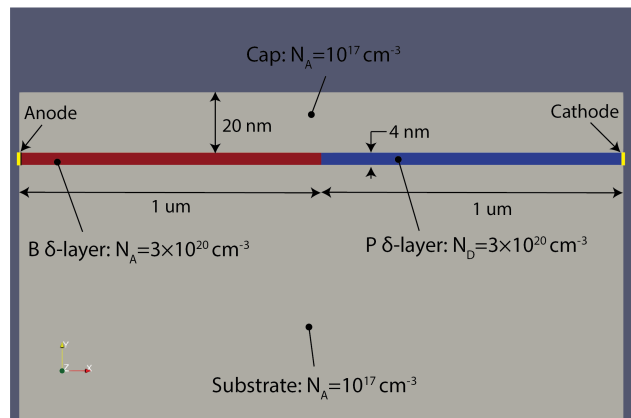


Figure 2. Schematic of the APAM pn junction device used in our simulations at low temperature. It consists of a δ layer-based pn junction. The δ -layers make direct Ohmic contact with the cathode and anode contacts as shown in the figure.

A. Band-to-band tunneling (BTBT)

A typical band edge profile of an APAM pn junction under different bias conditions are shown in Fig. 3. Panels (a, b, c) represent the band structure across the junction under equilibrium condition, as well as under reverse and forward biased conditions, respectively. It is seen that the valence band of the p-type δ region overlaps with the conduction band of the n-type δ region, enabling the BTBT when a voltage is applied to the junction. In reverse bias, when a negative voltage is applied to the anode contact (Fig. 3 b), the Fermi level of the anode contact increases in energy. This results in raising the valence and conduction bands of the p-type δ -layer to higher energies, enabling the electron-hole generation, i.e. the tunneling of electrons from the valence band in the p-type δ -layer to unoccupied states of the conduction band in the n-type δ -layer. Therefore, with increasing reverse voltages, BTBT current would keep increasing thanks to the increased overlap. From Fig. 1, we observe that the current increases monotonically with negative voltages, a clear indication of Zener tunneling.

Temperature (K)	30	50	75	100	300	4.5 (Measured values)
μ_e	326.97	244.44	194.14	164.95	89.34	40 ⁶
μ_h	201.76	150.83	119.78	101.76	55.05	20 ¹⁰
Eg (eV)	0.98	0.979	0.977	0.975	0.936	
χ (eV)	4.2198	4.2203	4.2213	4.2227	4.2422	

Table I. Electron (μ_e) and hole mobilities (μ_h) from Arora model, effective bandgap (Eg) and electron affinity (χ) for a doping density of $3 \times 10^{20} \text{ cm}^{-3}$. Last column includes the measured mobilities for electrons and holes in P and B δ -layers, respectively, from Refs. 6 and 10. The values of mobility are in the units of $\text{cm}^2\text{V}^{-1}\text{s}^{-1}$.

On the contrary, in forward bias, when a positive voltage is applied to the anode contact while the cathode is grounded (Fig. 3 c), the Fermi level of the anode contact decreases in energy. This causes the valence and conduction bands of the p-type δ -layer to shift to lower energies, enabling the electron-hole recombination, i.e. electrons from the conduction band in the n-type δ -layer tunnel into unoccupied states in the valence band in the p-type δ -layer. Quantum mechanically, the BTBT current is proportional to the product of electron and hole wavefunction overlap and the Fermi distribution. With increasing forward-biased voltages, the wavefunction overlap keeps decreasing, while the Fermi distribution increases due to the increasing Fermi level energy difference. The tunneling current is determined by the competing effect of the two factors. Initially, the increasing of Fermi distribution is more dominant, leading to the increase of tunneling current. As voltages increase, the reduction of wavefunction overlap shows more effect, which leads to decreasing of the current. Eventually the wavefunction approaches zero when the conduction and valence bands become misaligned.

The A and B parameters in the BTBT model (see Eq. 1) are related to material properties, such as effective masses and band gap³³⁻³⁵. These material properties can be significantly altered by the strong confinement and high doping densities of the dopants in the δ -layers, causing the values of the A and B parameter to differ substantially from those of bulk silicon. In the following, we evaluate how these parameters differ from bulk ones by fitting them with the experimental data from Ref. 10 for the forward bias conditions.

1. Forward response

In this section, we study the effect of BTBT on the I-V response for the APAM pn junction under forward bias, and examine the key different features between simulations and experimental data. For forward-biased simulations, though the BTBT model has no temperature dependence, several material models contain temperature dependence such as the Arora mobility model, the temperature-dependent band gap model, and the intrinsic concentration model described in Sec. II. To examine

the effect of temperature on the forward I-V curve, we simulated the APAM pn junction at various temperatures using the BTBT model with A and B values corresponding to bulk silicon. The key device parameters in the δ -layer at the various temperatures are listed in Table I. The simulated forward I-V curves are plotted in Fig. 4, where a negative differential conductance (NDC) region is clearly observed for voltages from 0 to 1 V. The NDC region is determined by BTBT and shows no temperature dependence as expected from the model. However, as proposed in Ref. 31, the temperature dependence in this model can be incorporated by adjusting the parameter B , which is proportional to $E_g^{3/2}$, while the parameter A can be approximately considered temperature-independent. On the other hand, in the above-threshold region, i.e. for voltages above 1 V, the normal diode behavior shows a temperature dependence mainly due to increase in the band gap with decreasing temperature as indicated in Table I. The temperature dependence becomes weaker for temperatures below 50 K. Hence, all following low-temperature simulations were done at 50 K unless otherwise noted. The voltage at which the current reaches a minimum in Fig. 4 is referred to as the valley voltage (a.k.a. threshold voltage) above which the diode behaves like a resistor. In theory, for heavily-doped silicon pn diode, this valley voltage should be nearly equal to the band-gap voltage, which is exactly what is observed in Fig. 4.

To further confirm that the NDC behavior in Fig. 4 is due to BTBT, we plot in Fig. 5 the BTBT generation rate spatial profiles near the pn junction region at 50 K for various voltages. One can observe that the BTBT recombination initially increases with increasing voltages, reaching its maximum magnitude at 0.26 V, corresponding to the peak in the IV curve shown in Fig. 4. Then, this increase in the magnitude of the BTBT recombination is followed by a decrease, corresponding to the decrease of the current in Fig. 4, and vanishing above the valley voltage. The reason for the non-monotonic change of the BTBT generation rate in the forward-biased region is due to the competing contributions from the field-dependent terms in Eq. (1). The first field factor term enforces zero BTBT under equilibrium conditions and its value increases with decreasing electric field, whereas other two field terms in Eq. (1) decrease

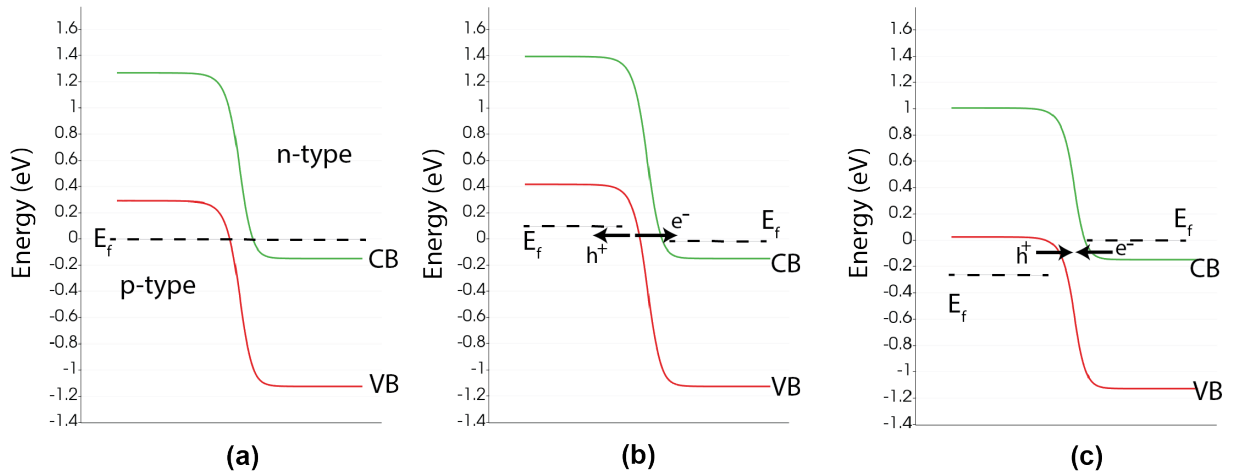


Figure 3. Band structure across the junction of an APAM pn device: (a) Band structure in equilibrium; (b) tunneling generation in reverse bias; and, (c) tunneling recombination in forward bias.

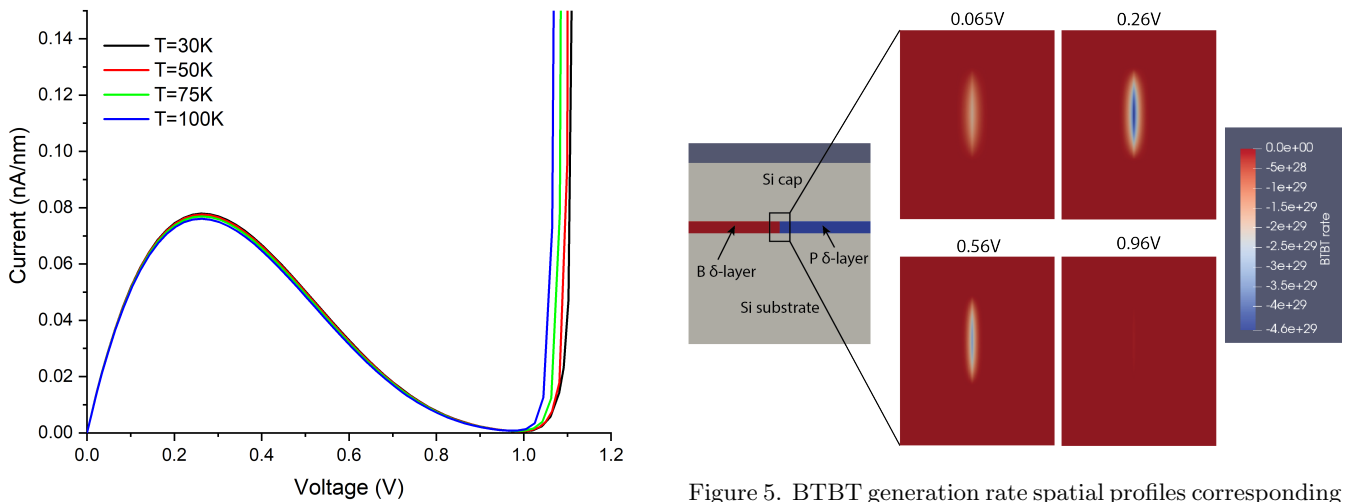


Figure 4. Simulated current-voltage (I-V) response of APAM pn device at several low temperatures under forward bias. $A = 1.0 \times 10^{19} \text{ cm}^{-3}\text{s}^{-1}$, $B = 3 \times 10^7 \text{ Vcm}^{-1}$, $\gamma=2$ and $\beta=1$.

with decreasing field. In the forward-biased regime, electric field in the junction keeps decreasing with increasing voltage. With decreasing field, the BTBT rate increases first because of the dominance of the first field factor term, and eventually decreases when the effects of other two field terms take over. The observed change of BTBT generation rate with increasing forward voltage aligns with the expected behavior described above for BTBT in highly doped pn junction, indicating that our local, field-dependent BTBT model can approximately capture the qualitative aspects of band-to-band tunneling in these systems. However, we also indicate that the model does exhibit some overestimation because it does not account for wavefunction overlap.

Fig. 6 includes an analysis of the effect of A and B parameters on the device response. From panel (a), cur-

Figure 5. BTBT generation rate spatial profiles corresponding to several voltages in Fig. 4. The BTBT rate is in unit of $\text{cm}^{-3}\text{s}^{-1}$.

rents in the NDC region increase proportionally with increasing A values, while the NDC peak-current voltages and valley voltages are not affected by different A values. From panel (b), it can be observed that currents in the NDC region increase as the B value decreases, and a smaller B value shifts the peak-current voltage and the valley voltage slightly to the right. Clearly, either an increase in A or decrease in B increases the BTBT generation rate according to Eq. (1), which subsequently increases tunneling current. However, neither the A nor the B value significantly affects the valley voltage, close enough to the measured value in Fig. 1.

Comparing the simulated forward I-V curve in Fig. 6 to the measured data, we observe two major differences: (i) the valley voltage in the measured data is much smaller than the theoretical value of about 1 V; (ii) the current suppression between 0 and 0.2 V in the data is not seen in the simulated curve. The question is what possible

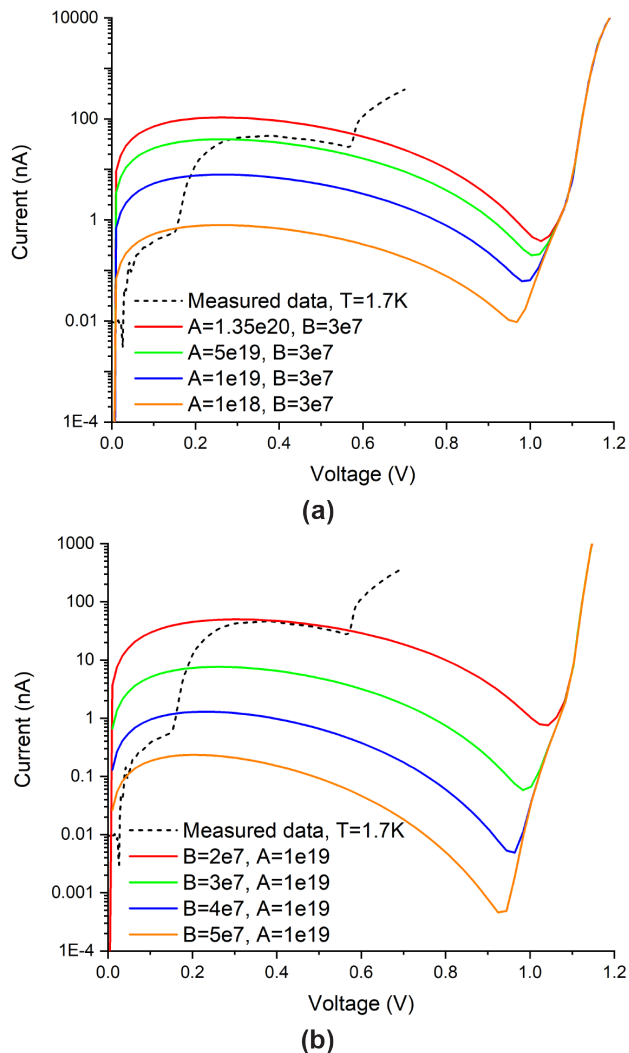


Figure 6. Simulated forward current-voltage (I-V) response. **(a)** For different values of the parameter A . **(b)** For different values of the parameter B . $\beta = 1$, and A and B parameters are in unit of $\text{cm}^{-3}\text{s}^{-1}$ and Vcm^{-1} , respectively. For comparison purposes, we multiplied the simulated currents in unit of A/cm by a width of the δ -layer of 100 nm, as given in Ref. 10.

physical mechanisms could cause these differences. In an attempt to address these questions, we have investigated three potential causes in the next subsections: (i) the effect of band-gap narrowing due to the δ -layer induced band structure change; (ii) the effect of non-ideal contact such as Schottky contact at the anode; and (iii) band quantization. Given the low temperatures used in the measurements in Ref. 10, we believe that TAT and leakage through cap and substrate are negligible because TAT requires phonons, which are more or less frozen below 50 K, and the Si cap and Si substrate are insulating according to our in-house experimental measurements at very low temperatures (below 30 K).

B. Effect of band gap narrowing

Band gap narrowing (BGN) is the reduction of the energy difference between the conduction band and the valence band in a semiconductor material caused by increasing the temperature and/or doping densities. In TCAD simulations, various models, such as the Slotboom model⁴⁷, have been employed to incorporate this effect. These models are known to work well for lightly to moderately doped semiconductors. However, they fail to accurately represent the impact of highly doped materials, such as in δ -layers. Additionally, they only consider the total doping density, without distinguishing between n-type or p-type dopants.

It is well known that the high doping densities in δ -layers significantly modify the electronic band structure, as observed in experiments^{36–40} and in quantum-mechanical simulations²⁴ for n-type δ -layers, and in DFT simulations for p-type δ -layers⁴⁵. To overcome the limitation of standard BGN models and account for the significant effect of BGN in δ -layers, we explore the potential impact of BGN in δ -layers using the model shown in Fig. 7(a). In contrast to standard models, the band gap in both δ layer regions are reduced with the doping density, but the electron affinity is modified only for the n-type δ -layer region. Fig. 7(b) shows the simulated I-V responses under forward voltages for different BGN values, with the same magnitude of BGN applied to both δ layer regions. From these results, we observe that, as the BGN value increases, the valley voltage decreases due to the band-gap reduction in the δ layers. This is accompanied with a reduction of current in the NDC region and a shift of the peak voltage towards lower values, which is because the magnitude of the electric field in the junction is reduced, leading to a decrease in the BTBT generation rate. Therefore, the BGN effect, caused by δ -layers that induced significant changes in the material's band structure, can plausibly explain the small valley voltage observed in the experimental APAM pn junction. The estimated magnitude of the BGN is also in very well agreement with ARPES measurements from Refs. 36 and 38.

In previous works^{20,50}, the observed lower valley voltage than the theoretically expected value in Si Esaki diode^{10,20} was explained by the existence of density of states in the band gap. These states facilitate the direct coherent tunneling, from gap state to gap state, leading to what they call "excess current". This current determines the valley voltage, and because it is driven by direct tunneling it is temperature independent⁵⁰. These states are always equilibrated with the corresponding Fermi levels. However, in highly doped system, e.g. δ -layer systems, those states becomes continuous in space, thus lowering/raising effectively the conduction/valence band edge and reducing the band gap. This observation substantiates our semi-classical approach of using the BGN effect to simulate the measured low valley voltage.

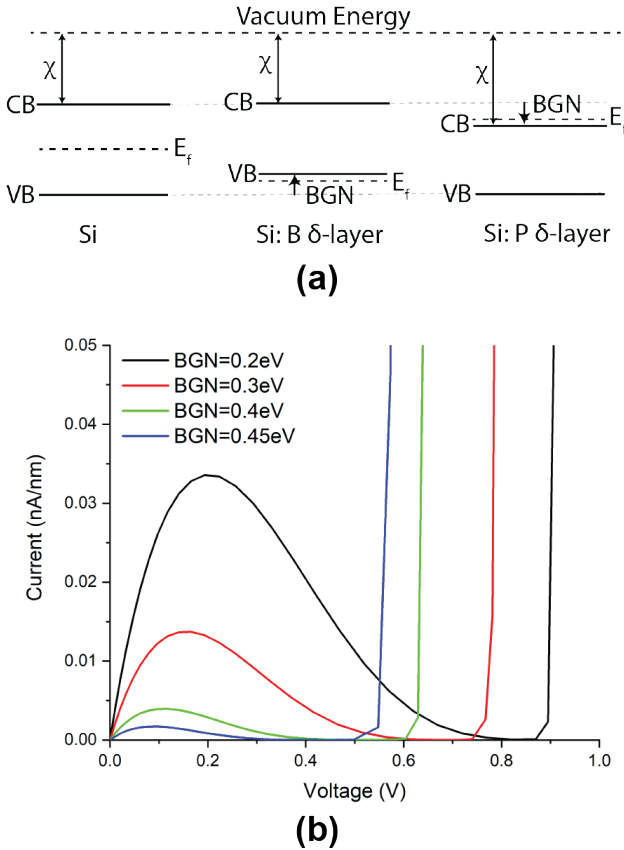


Figure 7. Effect of the band gap narrowing (BGN). (a) Schematic band diagram for the proposed BGN model within the p-type and n-type δ -layer regions; (b) Study of the effect of the corresponding BGN for the forward-bias response.

C. Effect of Schottky contact

Next, we investigate the effect of Schottky contact on the p-type side of the bipolar device, since the Schottky barrier is likely to be higher on that side. The existence of a Schottky barrier for holes at the junction between the metallic contact and the p-type δ -layer is due to the potential work function difference between them, being lower at the metal than at the p-type semiconductor. When applying a negative bias to the Schottky contact, the barrier for holes decreases, thus increasing the thermionic emission current; otherwise, when applying a positive bias to the Schottky contact, the barrier height for holes in the p-type semiconductor increases, thus reducing the thermionic emission current. However, for very highly doped semiconductors, tunneling plays an important role in the latter case, allowing holes to pass through the Schottky barrier. Higher doping density narrows the barrier width (i.e., the depletion region width), thereby increasing tunneling. Counterintuitively, with increasing positive bias, the barrier height increases, but the barrier width decreases, thereby enhancing the current through tunneling. We also note that, at low

temperature ($\lesssim 50$ K), the effect of temperature on the hole tunneling is negligible.

The first question to be addressed is whether the Schottky barrier is transparent to holes in very highly doped p-type δ -layers (e.g. $3 \times 10^{20} \text{ cm}^{-3}$), i.e., whether holes can tunnel through the barrier or are blocked. Fig. 8 a shows the Schottky contact resistance computed for a p-type δ -layer with Ohmic contact on one side and Schottky contact on the other side. The Schottky barrier height is around $1 \text{ eV} + V_{app}$, where V_{app} is the voltage applied to the contact. We note that, for very highly doped δ -layers, the resistance in the δ -layers is negligible, so the resistance in a is mainly due to the Schottky contact contribution. This result indicates that the overall contact resistance is small, being the Schottky barrier almost transparent to holes despite the high Schottky barrier. Additionally, as the bias increases, the Schottky resistance decreases further, enhancing the transparency of the barrier and facilitating hole tunneling.

For comparison, Fig. 8 b shows the resistance of the pn junction from Fig. 2 with Ohmic contact on both sides. Note that the pn junction resistance exhibits a peak corresponding to the valley voltage location. Comparing the magnitude of the resistance in both cases reveals that the pn junction resistance is generally at least one order of magnitude higher than the Schottky contact resistance. Therefore, Schottky contact is unlikely the reason for current suppression in the forward bias region.

D. Effect of band quantization

Our simulations show that we can use a combination of BTBT parameters and BGN to qualitatively approximate the experimental data. As shown in Fig. 9, our simulation results obtained using the BTBT parameters, $A = 1.0 \times 10^{19} \text{ cm}^{-3}\text{s}^{-1}$, $B = 2.0 \times 10^7 \text{ Vcm}^{-1}$ and $\beta = 1.5$, can capture the lower elbow of the I-V curve in the 0.0 to 0.2 voltage region, while the BTBT parameter set, $A = 1.0 \times 10^{19} \text{ cm}^{-3}\text{s}^{-1}$, $B = 2.0 \times 10^6 \text{ Vcm}^{-1}$ and $\beta = 4$, can capture the higher elbow of the I-V curve reasonably well (0.2 to 0.6 V). The low valley voltage is well modeled with a BGN value of 0.45 eV applied to the δ layers as shown in Fig. 7. We observe that using these two sets of BTBT parameters can qualitatively capture the two distinct forward I-V regions. This indicates that there may be two distinct BTBT regimes at work which can stem from band quantization and realignment of these quantized states. This result aligns very well with recent experimental^{39,40} and computational^{24,51} works. In these works, the existence of quantized conduction bands in n-type δ -layers and quantized valence bands in p-type δ layers was revealed. The band quantization was attributed to the strong confinement of dopants in one direction (a.k.a. size quantization). Additionally, in Refs. 24 and 51, it was found that the number of quasi-quantized states in n-type δ -layers, as well as the splitting energy between them, are strongly dependent on both the

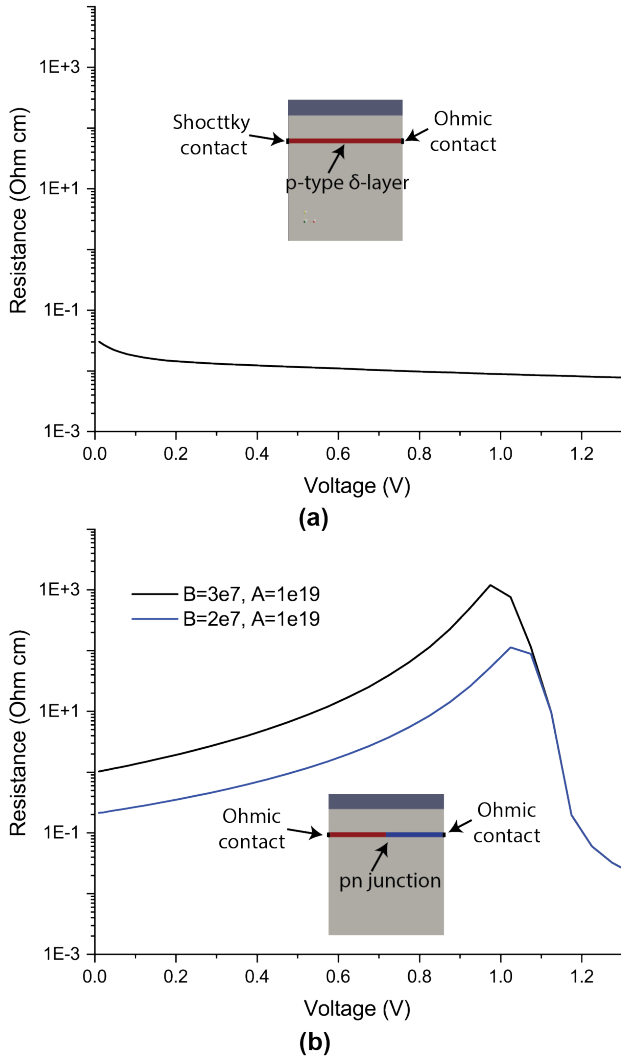


Figure 8. Study of the Schottky contact effect. **(a)** Schottky contact resistance between a metal and a very highly p-type doped δ -layer. **(b)** Resistance of the APAM pn junction. A and B parameters are in unit of $\text{cm}^{-3}\text{s}^{-1}$ and Vcm^{-1} , respectively. The metal work function W_f is 4.5 eV.

δ -layer thickness and the doping density.

To gain further understanding, a schematic representation of a possible combination of band quantization is shown in Fig. 10, assuming that only two quantized subbands exist in both conduction and valence band structure of the n-type and p-type δ -layer, respectively. The two shaded area in the valence band and conduction band represent the densities of occupied states for holes and electrons, respectively, in the two quantized subbands. As observed from the figure, initially, when a forward bias is applied, only two subbands overlap (see **(b)**). With a further increase in the bias, more subbands will be involved (see **(c)**), leading to a potential increase in the current. Thus, a very plausible explanation for the atypical behavior for Si Esaki diode, shown in region 2 and 3 in Fig. 1, might be attributed to the quantization of

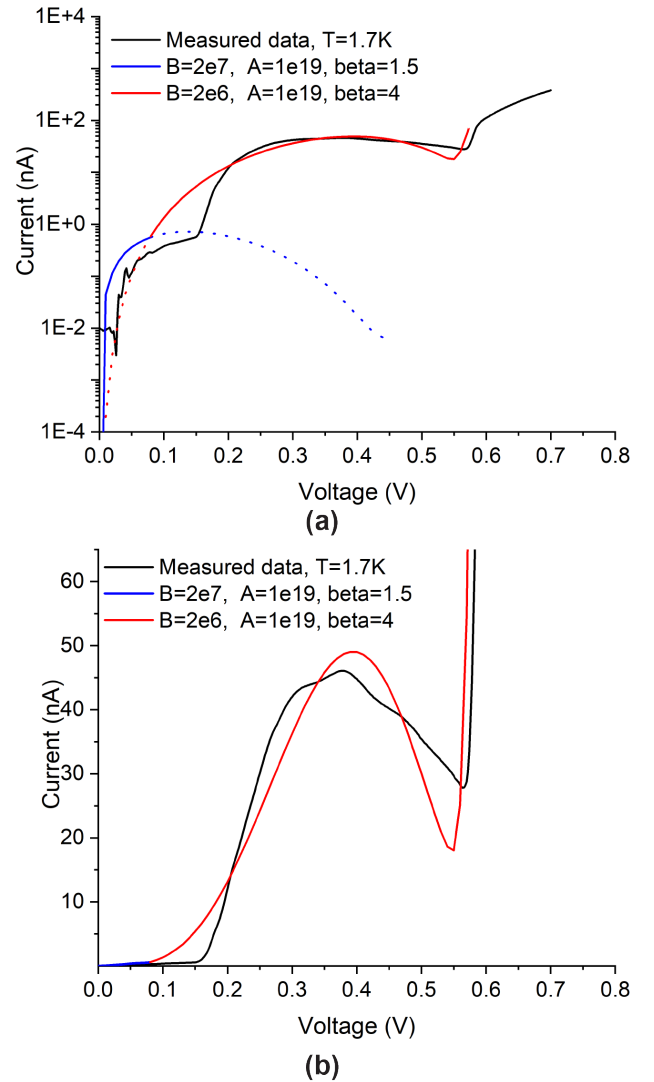


Figure 9. Comparing the simulated I-V response with the measured data with two set of fitted BTBT parameters and using the BGN model presented in Section III B with a BGN of 0.45 eV. **(a)** Semi-log scale, and **(b)** linear scale. A and B parameters are in unit of $\text{cm}^{-3}\text{s}^{-1}$ and Vcm^{-1} , respectively. For comparison purposes, we multiplied the simulated currents in unit of A/cm by a width of the δ -layer of 100 nm, as given in Ref. 10.

the band structure and the realignment of these quantized states. It is possible that the first BTBT region (0 to 0.2 volts) occurs when the lowest conduction subband and highest valence subband are aligned. As the applied voltage is increased, additional subbands become aligned allowing for increased BTBT, leading to the second BTBT region. This step-like behavior due to different band alignment has been reported in Germanium electron-hole bilayer tunnel FET⁵². Full quantum mechanical modeling of BTBT in an APAM pn junction in the future will clarify this hypothesis.

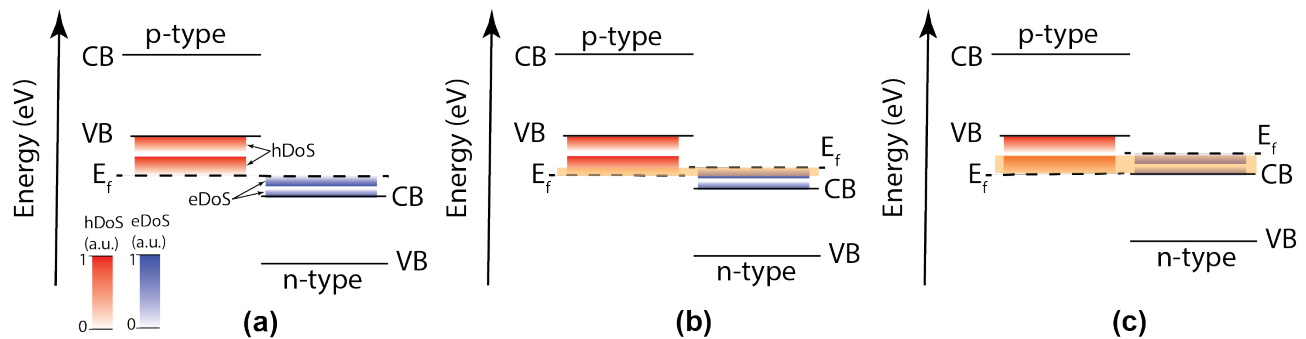


Figure 10. Quantization of the band structure in δ -layers. The figure represents the band structure across the pn junction: (a) band structure in equilibrium; (b) after applying a small forward bias of V_0 ; and, (c) after applying an higher forward bias $V_1 > V_0$. hDoS represents the hole density of states, while eDoS represents the electron density of states. The yellow highlight represents the overlaps between hole states and electron states.

IV. ROOM-TEMPERATURE TRANSPORT MECHANISMS

At room temperature, other mechanisms apart from BTBT can be relevant in these devices, such as trap-assisted tunneling (TAT) via phonon interaction and current leakage through the cap and substrate. Electron-hole pairs can recombine/generate via the interaction with the lattice and with the assistance of existing defects near a junction. Similarly, dopants in the Si cap and Si substrate can be active, contributing to well-known potential current leakage pathway. In the following subsections, we evaluate the effect of TAT and current leakage on the device characteristic at room temperature.

A. Trap-assisted tunneling

At room temperature, trap-assisted tunneling (TAT) due to phonon interaction can become relevant near the pn junction. We believe this tunneling mechanism is negligible at low temperatures (e.g., below 50 K) due to the freezing of phonons, but it can become appreciable at higher temperatures. For our simulations, we use the Schenk's TAT model⁵³ implemented in Charon software. A summary of the model implementation is included in Appendix A. The following tunneling relevant parameters are kept constant in our simulations: Huang-Rhys factor of 3.5 and the optical phonon energy is assumed to be $\hbar\omega = 68$ meV.

Fig. 11 depicts the simulated I-V forward responses including TAT near the junction for different trap energy levels in (a) and for different carrier lifetimes in (b). We note that the trap energy in this model is with respect to the conduction band edge. Interestingly, the simulated I-V curves show three distinct regions: (i) currents in the low voltages are determined by BTBT; (ii) currents in

the medium voltages are dominant by TAT, showing a strong dependence on TAT model parameters; (iii) currents in the high voltages result from the resistor-like response. These results show that TAT rates decrease for shallower trap defects, i.e., traps with energy levels closer to the conduction band edge. This is consistent with the fact that deep-level traps are more efficient recombination centers. In addition, TAT rates decrease as the carrier lifetimes become larger. The lifetime is inversely related to the number of defects near the junction, i.e. the lower defect density, the higher lifetime of the carrier.

The Poole-Frenkel effect, which describes how the effective depth of a trap is reduced due to the Coulomb interaction between a free carrier and the trap, is not taken into account in our TAT model. However, it is important to note that this effect is weaker than the tunneling effect at a strong electric fields, whereas it might moderately enhance the emission probability at weak electric fields, and thus influence the net recombination rate³¹. Given that the built-in electric field across the pn junction in our device is very high, we expect that the Poole-Frenkel effect on the device response will be minimal at very low forward biases, and it might only slightly enhance the current in the voltage range where the TAT is significant.

From these results, it is evident that the effect of TAT will decrease as the the junction becomes more ideal. Conversely, it can become the dominant mechanism if there are a considerable number of defects near the junction. Therefore, from this simulation study, we predict that, as APAM pn devices become more mature to operate at room temperatures, complex I-V responses may appear due to interplay of BTBT and TAT transport mechanisms in these devices.

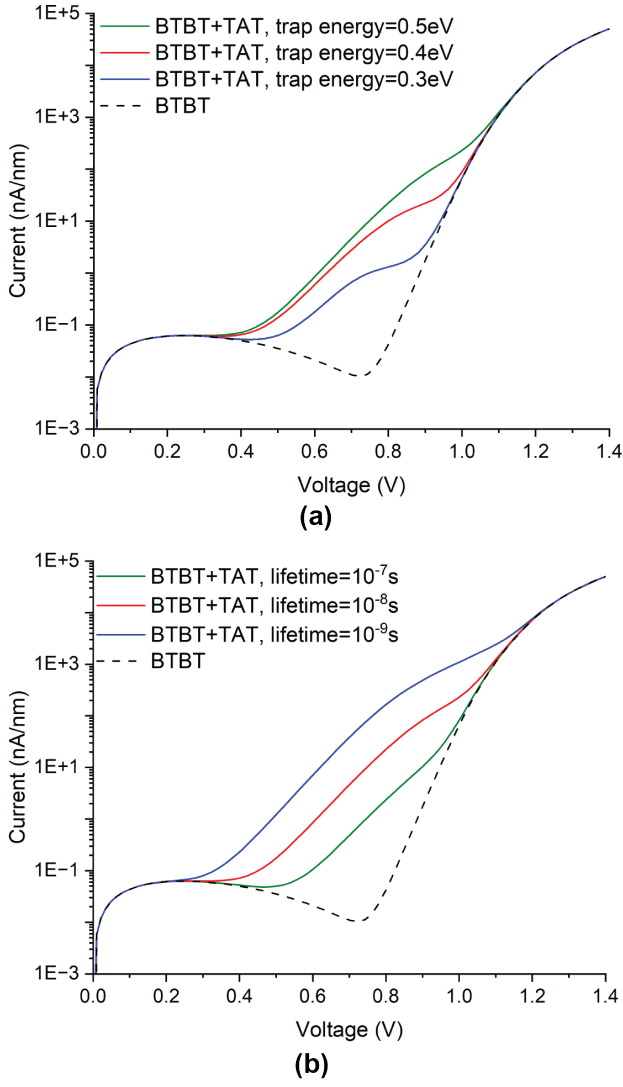


Figure 11. Study of trap assisted band tunneling (TAT) at room temperature in APAM pn junctions: **(a)** Effect of trap energy levels, and **(b)** Effect of lifetimes. BTBT parameters used in the simulations are: $A = 1 \times 10^{19} \text{ cm}^{-3}\text{s}^{-1}$, $B = 3 \times 10^7 \text{ V/cm}$, and $\beta = 1.5$. Default values for the parameters in the TAT model are: lifetimes $\tau_{n0} = \tau_{p0} = 10^{-8} \text{ s}$, and trap energy level $E_t = 0.5 \text{ V}$. Details of the TAT parameters can be found in Appendix A.

B. Current leakage study

Leakage across the Si substrate or cap is minimal at very low temperatures, since dopants are inactive in these regions at these temperatures. This observation has been confirmed in our experiments and in Ref. 10. However, at room temperature, dopants in the cap and in the substrate can be activated, resulting not only in current paths across the δ -layers, but also across the Si cap and Si substrate. Thus, it is important to discern the effect of possible current leakage on the device response at room temperature. We explore two distinct configurations as

shown in Fig. 12: in **(a)**, two metal contacts touch the pn junction on both sides, while in **(b)**, the p-type/n-type implants makes contact with the B/P-doped δ layers, respectively.

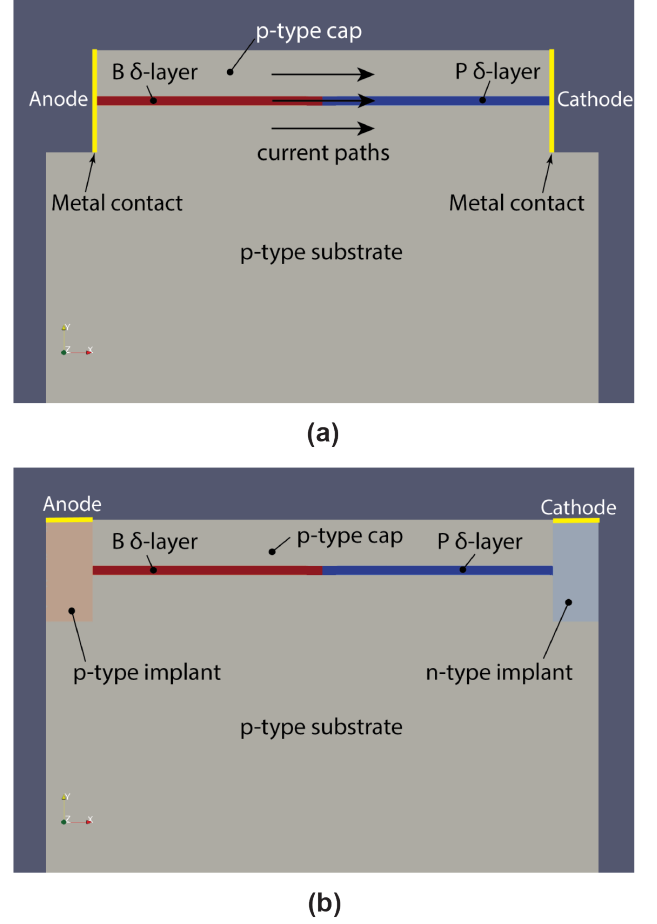


Figure 12. APAM pn junction devices used for the room temperature simulations: **(a)** with metal contacts; and **(b)** with highly doped n-type and p-type implants.

Fig. 13 includes the I-V responses for both contact configurations. We observe significantly different behavior in the device response, highlighting the strong dependence on the contact configurations at room temperature. For the metallic contact, as expected, the current leakage through the cap and the substrate is significant (illustrated in Fig. 12 **(a)** by arrows). This leakage dismisses the NDC and the Esaki behavior of the pn device, resulting in a response similar to that of a resistor. However, for the configuration with doped implants, the I-V response maintains the NDC behavior, indicating a negligible or minimal current leakage for low forward biases, with current paths primarily across the δ -layers, as reflected in the figure when comparing with the IV curve of the ideal device in Fig. 2 at room temperature. For the configuration with doped implants, the pn junction formed between the p-type cap/substrate and the n-type implant prevents an excess current leakage in

the NDC-dominant low-voltage regime. However, this parallel pn junction exhibits leakage current at higher positive voltages, which is why the current for the solid blue curve is higher than the dashed black curve in the above-threshold voltage region, resulting in a lower valley voltage. This is primarily due to the fact that the barrier between the p-type cap/substrate and n-type implant is smaller than that of the δ -layer pn junction. Note also that the valley voltage for the ideal device at room temperature, as indicated by the dashed black curve, occurs at lower voltages, around 0.7 V, c.f. Fig. 4, due to the effect of temperature. In conclusion, the performance of APAM devices can be significantly impacted by leakage through the substrate/cap at room temperature. Therefore, when designing APAM devices for room-temperature operation, it is crucial to isolate the substrate/cap region from the metallic contact to minimize leakage.

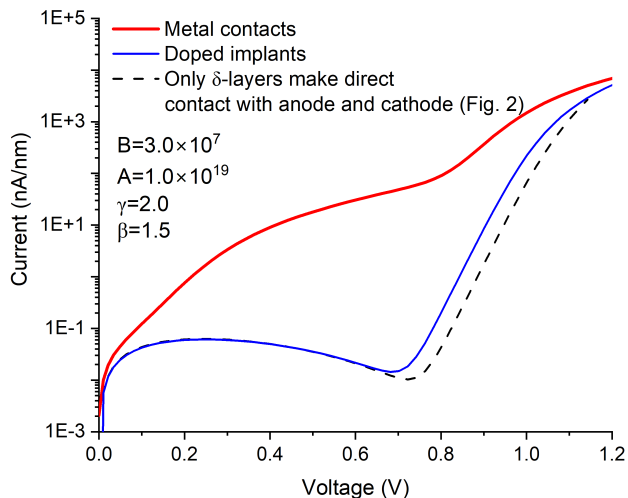


Figure 13. Study of the current leakage at room temperature for the configurations presented in Fig. 12. A and B parameters are in unit of $\text{cm}^{-3}\text{s}^{-1}$ and Vcm^{-1} , respectively.

V. CONCLUSIONS

In this work, we investigated the transport mechanisms that can occur in APAM pn junctions at cryogenic and room temperatures using TCAD simulations. We also explored the possible mechanisms behind the anomalous behavior in the forward-bias response observed in recent measurements¹⁰ at cryogenic temperatures, which deviates from the typical forward-bias response of an Esaki-type diode. These anomalous behaviors include current suppression at low voltages in the forward-bias response and a very low valley voltage at cryogenic temperatures. We found that the low valley voltage can be the result of the band-gap narrowing due to the strong confinements of the dopants in the δ -layers that modify the electronic band structures. We propose a band-gap

narrowing (BGN) model that can account for this effect within convectional TCAD simulations. We also found that using a combination of BTBT parameters, we can approximate the current suppression and the NDC behavior. This indicates that there may be two distinct BTBT regimes at work, which can stem from band quantization and realignment due to strong potential confinement in the δ layers. Finally, we predicted that TAT and current leakage might play an important role at room temperature. As APAM pn devices become more mature to operate at room temperatures, complex I-V responses may appear due to interplay of BTBT, TAT and current leakage in these devices.

ACKNOWLEDGMENTS

This work was supported, in part, by the LPS Quantum Collaboratory and, in part, by the Laboratory Directed Research and Development (LDRD) program at Sandia National Laboratories. Sandia National Laboratories is a multimission laboratory managed and operated by National Technology and Engineering Solutions of Sandia, LLC., a wholly owned subsidiary of Honeywell International, Inc., for the U.S. Department of Energy's National Nuclear Security Administration under contract DE-NA-0003525. This paper describes objective technical results and analysis. Any subjective views or opinions that might be expressed in the paper do not necessarily represent the views of the U.S. Department of Energy or the United States Government.

AUTHOR DECLARATIONS

Conflict of Interest

The authors have no conflicts to disclose.

Author Contributions

J.P. Mendez, and X. Gao: Conceptualization (equal); Data curation (equal); Formal analysis (equal); Investigation (equal); Visualization (equal); Writing – original draft (equal); Writing – review & editing (equal); Methodology (equal); Software (equal); **J. Ivie, and S. Misra:** Conceptualization (equal); Formal analysis (equal); Investigation (supporting); Writing – original draft (equal); Writing – review & editing (equal); Methodology (equal); **J.H.G Owen, W.P. Kirk, and J.N. Randall:** Conceptualization (equal); Formal analysis (supporting); Investigation (supporting); Writing – review & editing (supporting); Methodology (supporting).

DATA AVAILABILITY

The data that support the findings of this study are available from the corresponding author upon reasonable request

REFERENCES

- ¹H. F. Wilson, O. Warschkow, N. A. Marks, N. J. Curson, S. R. Schofield, T. C. G. Reusch, M. W. Radny, P. V. Smith, D. R. McKenzie, and M. Y. Simmons, *Phys. Rev. B* **74**, 195310 (2006).
- ²O. Warschkow, N. J. Curson, S. R. Schofield, N. A. Marks, H. F. Wilson, M. W. Radny, P. V. Smith, T. C. G. Reusch, D. R. McKenzie, and M. Y. Simmons, *The Journal of Chemical Physics* **144**, 014705 (2016).
- ³M. Fuechsle, J. Miwa, and S. Mahapatra et al., *Nature Nanotech.* **7**, 242 (2012).
- ⁴J. A. Ivie, Q. Campbell, J. C. Koepke, M. I. Brickson, P. A. Schultz, R. P. Muller, A. M. Mounce, D. R. Ward, M. S. Carroll, E. Bussmann, A. D. Baczewski, and S. Misra, *Phys. Rev. Applied* **16**, 054037 (2021).
- ⁵J. Wyrick, X. Wang, P. Namboodiri, R. V. Kashid, F. Fei, J. Fox, and R. Silver, *ACS Nano* **16**, 19114 (2022).
- ⁶K. E. J. Goh, L. Oberbeck, M. Y. Simmons, A. R. Hamilton, and M. J. Butcher, *Phys. Rev. B* **73**, 035401 (2006).
- ⁷B. Weber, S. Mahapatra, H. Ryu, S. Lee, A. Fuhrer, T. C. G. Reusch, D. L. Thompson, W. C. T. Lee, G. Klimeck, L. C. L. Hollenberg, and M. Y. Simmons, *Science* **335**, 64 (2012).
- ⁸S. R. McKibbin, G. Scappucci, W. Pok, and M. Y. Simmons, *Nanotechnology* **24**, 045303 (2013).
- ⁹J. G. Keizer, S. R. McKibbin, and M. Y. Simmons, *ACS Nano* **9**, 7080 (2015).
- ¹⁰T. Škřeň, S. A. Köster, B. Douhard, C. Fleischmann, and A. Fuhrer, *Nature Electronics* **3**, 524 (2020).
- ¹¹K. J. Dwyer, S. Baek, A. Farzaneh, M. Dreyer, J. R. Williams, and R. E. Butera, *ACS Applied Materials & Interfaces* **13**, 41275 (2021).
- ¹²S. Mahapatra, H. Büch, and M. Y. Simmons, *Nano Letters* **11**, 4376 (2011).
- ¹³M. G. House, E. Peretz, J. G. Keizer, S. J. Hile, and M. Y. Simmons, *Applied Physics Letters* **104**, 113111 (2014).
- ¹⁴X. Gao, J. P. Mendez, T.-M. Lu, E. M. Anderson, D. M. Campbell, J. A. Ivie, S. W. Schmucker, A. Grine, P. Lu, L. A. Tracy, R. Arghavani, and S. Misra, in *2021 International Conference on Simulation of Semiconductor Processes and Devices (SISPAD)* (2021) pp. 102–106.
- ¹⁵M. B. Donnelly, J. G. Keizer, Y. Chung, and M. Y. Simmons, *Nano Letters* **21**, 10092 (2021).
- ¹⁶F. Krauth, S. Gorman, Y. He, M. Jones, P. Macha, S. Kocsis, C. Chua, B. Voisin, S. Rogge, R. Rahman, Y. Chung, and M. Simmons, *Phys. Rev. Appl.* **17**, 054006 (2022).
- ¹⁷L. Fricke, S. J. Hile, L. Kranz, Y. Chung, Y. He, P. Pakkiam, M. G. House, J. G. Keizer, and M. Y. Simmons, *Nature Communications* **12**, 3323 (2021).
- ¹⁸X. Wang, E. Khatami, F. Fei, J. Wyrick, P. Namboodiri, R. Kashid, A. F. Rigosi, G. Bryant, and R. Silver, *Nature Communications* **13**, 6824 (2022).
- ¹⁹M. Kiczynski, S. K. Gorman, H. Geng, M. B. Donnelly, Y. Chung, Y. He, J. G. Keizer, and M. Y. Simmons, *Nature* **606**, 694 (2022).
- ²⁰A. G. Chynoweth, W. L. Feldmann, and R. A. Logan, *Phys. Rev.* **121**, 684 (1961).
- ²¹M. Oehme, D. Hähnel, J. Werner, M. Kaschel, O. Kirfel, E. Kasper, and J. Schulze, *Applied Physics Letters* **95**, 242109 (2009), <https://pubs.aip.org/aip/apl/article-pdf/doi/10.1063/1.3274136/14422209/242109.1.online.pdf>.
- ²²H. Schmid, C. Bessire, M. T. Björk, A. Schenk, and H. Riel, *Nano Letters* **12**, 699 (2012), pMID: 22214422, <https://doi.org/10.1021/nl2035964>.
- ²³<https://charon.sandia.gov/>.
- ²⁴D. Mamaluy, J. P. Mendez, X. Gao, and S. Misra, *Communications Physics* **4**, 205 (2021).
- ²⁵X. Gao, L. A. Tracy, E. M. Anderson, D. M. Campbell, J. A. Ivie, T.-M. Lu, D. Mamaluy, S. W. Schmucker, and S. Misra, in *2020 International Conference on Simulation of Semiconductor Processes and Devices (SISPAD)* (2020) pp. 277–280.
- ²⁶A. N. Brooks and T. J. Hughes, *Computer Methods in Applied Mechanics and Engineering* **32**, 199 (1982).
- ²⁷P. Bochev and K. Peterson, *Open Mathematics* **11**, 1458 (2013).
- ²⁸P. Bochev, K. Peterson, and X. Gao, *Computer Methods in Applied Mechanics and Engineering* **254**, 126 (2013).
- ²⁹<https://cubit.sandia.gov>.
- ³⁰<https://paraview.org>.
- ³¹G. Hurkx, D. Klaassen, and M. Knuvers, *IEEE Transactions on Electron Devices* **39**, 331 (1992).
- ³²H.-Y. Wong, D. Dolgos, L. Smith, and R. V. Mickevicius, *Microelectronics Reliability* **104**, 113552 (2020).
- ³³K.-H. Kao, A. S. Verhulst, W. G. Vandenberghe, B. Sorée, G. Groeseneken, and K. De Meyer, *IEEE Transactions on Electron Devices* **59**, 292 (2012).
- ³⁴E. Kane, *Journal of Physics and Chemistry of Solids* **12**, 181 (1960).
- ³⁵W. Vandenberghe, B. Sorée, W. Magnus, and G. Groeseneken, *Journal of Applied Physics* **107**, 054520 (2010), <https://pubs.aip.org/aip/jap/article-pdf/doi/10.1063/1.3311550/15057390/054520.1.online.pdf>.
- ³⁶J. A. Miwa, P. Hofmann, M. Y. Simmons, and J. W. Wells, *Phys. Rev. Lett.* **110**, 136801 (2013).
- ³⁷J. A. Miwa, O. Warschkow, D. J. Carter, N. A. Marks, F. Mazzola, M. Y. Simmons, and J. W. Wells, *Nano Letters* **14**, 1515 (2014), pMID: 24571617, <https://doi.org/10.1021/nl404738j>.
- ³⁸F. Mazzola, J. W. Wells, A. C. Pakpour-Tabrizi, R. B. Jackman, B. Thiagarajan, P. Hofmann, and J. A. Miwa, *Phys. Rev. Lett.* **120**, 046403 (2018).
- ³⁹A. J. Holt, S. K. Mahatha, R.-M. Stan, F. S. Strand, T. Nyborg, D. Curcio, A. K. Schenk, S. P. Cooil, M. Bianchi, J. W. Wells, P. Hofmann, and J. A. Miwa, *Phys. Rev. B* **101**, 121402 (2020).
- ⁴⁰F. Mazzola, C.-Y. Chen, R. Rahman, X.-G. Zhu, C. M. Polley, T. Balasubramanian, P. D. C. King, P. Hofmann, J. A. Miwa, and J. W. Wells, *npj Quantum Materials* **5**, 34 (2020).
- ⁴¹D. J. Carter, O. Warschkow, N. A. Marks, and D. R. McKenzie, *Phys. Rev. B* **79**, 033204 (2009).
- ⁴²D. J. Carter, N. A. Marks, O. Warschkow, and D. R. McKenzie, *Nanotechnology* **22**, 065701 (2011).
- ⁴³S. Lee, H. Ryu, H. Campbell, L. C. L. Hollenberg, M. Y. Simmons, and G. Klimeck, *Phys. Rev. B* **84**, 205309 (2011).
- ⁴⁴D. W. Drumm, A. Budi, M. C. Per, S. P. Russo, and L. C. L. Hollenberg, *Nanoscale Research Letters* **8**, 111 (2013).
- ⁴⁵Q. T. Campbell, S. Misra, and A. D. Baczewski, *Journal of Applied Physics* **134**, 044401 (2023), <https://pubs.aip.org/aip/jap/article-pdf/doi/10.1063/5.0156832/18058355/044401.1.5.0156832.pdf>.
- ⁴⁶N. Arora, J. Hauser, and D. Roulston, *IEEE Transactions on Electron Devices* **29**, 292 (1982).
- ⁴⁷J. Slotboom, *Solid-State Electronics* **20**, 279 (1977).
- ⁴⁸L. Musson, G. Hennigan, X. Gao, R. Humphreys, M. Negoita, and A. Huang, “Charon user manual: v. 2.2 (revision1),” Tech. Rep. (United States, 2022).
- ⁴⁹Unpublished in-house measurements on device structures similar to Ref. 10 were investigated and used as empirical evidence in parts of the following analysis.
- ⁵⁰C. Rivas, R. Lake, W. R. Frenley, G. Klimeck, P. E. Thompson, K. D. Hobart, S. L. Rommel, and P. R. Berger, *Journal of Applied Physics* **94**, 5005 (2003), <https://pubs.aip.org/aip/jap/article-pdf/94/8/5005/18705824/5005.1.online.pdf>.
- ⁵¹J. P. Mendez and D. Mamaluy, *Scientific Reports* **12**, 16397 (2022).

⁵²C. Alper, L. Lattanzio, L. De Michielis, P. Palestri, L. Selmi, and A. M. Ionescu, IEEE Transactions on Electron Devices **60**, 2754 (2013).

⁵³A. Schenk, Solid-State Electronics **35**, 1585 (1992).

⁵⁴X. Gao, B. Kerr, and A. Huang, Journal of Applied Physics **125**, 054503 (2019), https://pubs.aip.org/aip/jap/article-pdf/doi/10.1063/1.5078685/13678824/054503.1_online.pdf.

Appendix A: Trap-assisted tunneling (TAT) model

For traps nor located in the mid-band gap, the recombination rate⁵⁴ can be expresses as

$$R_{tat} = \sum_j \frac{np - n_{ie}^2}{\tau_p^j(n + n_t^j) + \tau_n^j(p + p_t^j)} \quad (\text{A1})$$

where the summation runs over the total number of different types of traps, n_{ie} is the effective intrinsic concentration of the material, n_t^j and p_t^j for the j-th type of trap

are equal to

$$n_t^j = N_C \exp\left(-\frac{E_t^j}{k_B T}\right), \quad p_t^j = N_V \exp\left(-\frac{E_g - E_t^j}{k_B T}\right) \quad (\text{A2})$$

where N_C and N_V are the effective density of states in the conduction and valence bands, respectively, E_t^j is the j-th trap energy measured from the conduction band edge, E_g is the effective band gap, k_B is the Boltzmann constant, and T is the lattice temperature. The lifetimes τ_n^j and τ_p^j depend on the lattice temperature and the electric field

$$\tau_n^j(T, F) = \frac{\tau_{n0}^j}{1 + g_n^j(T, F)}, \quad \tau_p^j(T, F) = \frac{\tau_{p0}^j}{1 + g_p^j(T, F)} \quad (\text{A3})$$

where τ_{n0}^j and τ_{p0}^j are field-independent lifetimes, and $g_n^j(T, F)$ and $g_p^j(T, F)$ are the electron and hole field enhancement factors, which capture the recombination enhancement due to band-to-trap tunneling.